Hubble Space Telescope Observations of Active Asteroid (101955) Bennu

David Jewitt[1], Max Mutchler[2], and Yoonyoung Kim[1]

[1]Department of Earth, Planetary and Space Sciences, UCLA, 595 Charles Young Drive, Los Angeles, CA 90095

[2]Space Telescope Science Institute, Baltimore, MD 21218

djewitt@gmail.com

Received _____; accepted _____

Revised October 3

ABSTRACT

Measurements from NASA's OSIRIS-REx spacecraft revealed (101955) Bennu as a member of the active asteroid class. These objects exhibit transient, comet-like activity, commonly producing particle trails best observed from a vantage point close to the projected orbit plane. Accordingly, we obtained deep, high resolution observations of Bennu at orbit plane crossing in 2023, using the Hubble Space Telescope. We find no evidence for ejected material, and place model-dependent limits to the mass loss of $dM/dt < 0.12$ kg s^{-1} from an analysis of the near-nucleus surface brightness profiles and $dM/dt < 6 \times 10^{-3}$ kg s^{-1} from the absence of a measurable particle trail. These limits are one to two orders of magnitude smaller than rates of mass loss measured remotely in other active asteroids and raise the possibility that low activity in many or most asteroids might fall beneath the prevailing thresholds offered by remote observations. Taking a still smaller mass loss rate estimated from OSIRIS-REx data, we calculate a specific rate $\mathcal{L} \sim 10^{-7}$ [kg km^{-2} s^{-1}] and extrapolate to the entire main-belt asteroid population. We estimate a cumulative dust production rate $\sim 850 r_{min}^{-1/2}$ [kg s^{-1}], where r_{min} is the minimum asteroid radius in meters. For $r_{min} > 1$ m, this is <1% to 10% of the rate needed to sustain the Zodiacal cloud in steady state.

1. INTRODUCTION

Asteroids and comets, formerly thought to be distinct products of accretion on either side of the snow line, are now recognized as end members of a continuum (Jewitt & Hsieh 2024). In between the extremes, a few dozen bodies are known to have asteroidal orbits (Tisserand parameters with respect to Jupiter $T_J \gtrsim 3.08$) while showing comet-like

morphologies. These so-called "active asteroids" appear comet-like as a result of their intermittent ejection of dust. A surprising number of physical mechanisms behind the ejection have been identified. Some active asteroids are indeed icy bodies (these are the "main belt comets"; Hsieh & Jewitt (2006)), in which subsurface ice sublimates when exposed by the sudden removal of a refractory debris mantle. Others are produced by collisional shattering, impact ejection, thermal fatigue, and still others are products of rotational instability, driven either by torques from radiation or from anisotropic outgassing (Jewitt 2012).

Observations from NASA's OSIRIS-REx mission show that near-Earth asteroid (101955) Bennu (formerly 1999 RQ36) is an active asteroid, episodically ejecting centimeter-sized particles with speeds from a few cm s^{-1} to $\sim$3 m s^{-1} (Lauretta et al. (2019a), Lauretta et al. (2019b), Chesley et al. (2020)). The process responsible for the ejection remains unknown, with possible mechanisms being a subset of those already invoked to account for the active asteroids (Jewitt 2012). Specifically, thermal fracture (Molaro et al. 2020), electrostatic launch (Hartzell et al. 2022), and impact of micrometeoroids (Bottke et al. 2020) have all been considered as possible mechanisms on Bennu. Ice sublimation seems unlikely given Bennu's proximity to the Sun and resulting mean blackbody temperature, T = 260 K, which is far too high for water ice or other common volatiles to persist near the surface.

The orbit of Bennu has semimajor axis a = 1.126 AU, eccentricity e = 0.204 and inclination i = 6.0°, giving a Tisserand parameter with respect to Jupiter, $T_J = 5.525$. The perihelion lies interior to the Earth's orbit at q = 0.897 AU while aphelion, Q = 1.356 AU, is interior to the orbit of Mars and to the main asteroid belt from which Bennu is now dynamically decoupled. Pre-spacecraft spectroscopic measurements indicated a B-type (i.e., optically blue) surface, suggesting minimal thermal alteration and the presence of hydrated

minerals. These properties, and easy access to Bennu from Earth-launched spacecraft, were the motivation for NASA's OSIRIS-REx mission. Samples returned from this mission confirm the volatile rich nature and suggest a distant origin for Bennu, in the middle or outer solar system (Nuth et al. (2020), Glavin et al. (2025)).

Bennu is small, with an effective diameter of only ∼0.5 km (Lauretta et al. 2019a). Sub-kilometer sized objects in the main asteroid belt have collisional lifetimes that are short compared to the age of the solar system, and their existence implies that they are fragments of a once larger body. Bennu is possibly an escapee from the Polana-Eulalia collisional complex at $r_H \sim 2.4$ au (Walsh et al. (2013), Takir et al. (2024)) and it is reportedly a second generation rubble pile, having been fragmented and re-formed at least once since its original collision (Walsh et al. 2024). Both the blocky surface and the internal porosity implied by Bennu's low bulk density ($\rho_B = 1190 \pm 15$ kg m^{-3}; Goossens et al. (2021)) are consistent with a rubble pile structure. In addition, the diamond-like or "top-shaped" body of Bennu, produced by the equator-ward movement of material from the polar regions under centripetal acceleration, also reflects a fragmented and weak interior (Roberts et al. 2021). The present rotational period is 4.3 hours and, given its low density, Bennu remains close to rotational instability, where centripetal forces at the equator rival those of self-gravity.

The centimeter-sized particles detected at Bennu are individually 10 to 100 times larger (i.e., 10^3 to 10^6 times more massive) than the 0.1 mm to 1 mm particles inferred to dominate mass loss in most active asteroids. This difference is plausibly interpreted as an observational artifact because the cameras on OSIRIS-REx lack the sensitivity to detect particles much smaller than centimeter size. Conversely, small numbers of centimeter sized particles would not be detectable in ground-based observations, highlighting the mismatch between the sensitivity to asteroid activity of space-based and ground-based observations.

Hergenrother et al. (2020) concluded that material ejected from Bennu could not be

detected in remote telescopic observations if the mass loss rate remains steady. However, observations of other active asteroids show that the mass loss is generally episodic, with order of magnitude variations occuring on timescales from days to years (Jewitt (2012), Jewitt & Hsieh (2024)). They also show that debris trails, consisting of large, slow-moving particles, are most prominent when observed from close to the projected orbit plane. In this paper we analyze archival data and present new, highly sensitive, high resolution Hubble Space Telescope observations of Bennu taken from near the projected orbital plane.

2. Observations

Here, we consider three sets of observations from the Hubble Space Telescope (HST). First, we use archival observations from 2012 (Cycle 19, Program GO 13118, PI: M. Nolan). Observations from this program were taken to study the rotation of Bennu and have been used to obtain a 2.5σ detection of rotational spin-up (Nolan et al. 2019). Observations under GO 13118 were obtained at two epochs, in 2012 September and 2012 December. Second, we use new data from 2023 (Cycle 31, Program GO 17215, PI: Jewitt). The observations were obtained on three dates (UT 2023 September 24, 25 and 26) but those on the 26th were found to have mis-pointed as a result of guide star acquisition failure, so only data from September 24 and 25 are useful. All HST observations employed the WFC3 camera (image scale $0.04''$ pixel^{-1}) and the F350LP filter, which provides maximum sensitivity to faint emission. The latter is a long-pass filter with an extremely broad (equivalent width 4800Å) passband, giving an effective wavelength near 6230Å when observing a source with a Sun-like spectrum.

Table 1 summarizes the geometry of observation on each date of observation. The observing geometries differ significantly between sets. Notably, visits in 2023 September were timed to correspond to the crossing of the orbital plane of Bennu. Observations from

this perspective provide maximum sensitivity to large particles which are confined by their low velocities to be close to the orbital plane.

2.1. Composite Images

We reduced the data according to the following procedure. Each image was visually examined to assess the impact of field stars and galaxies trailed relative to Bennu by the non-sidereal (largely parallactic) motion of the telescope. Angular rates of Bennu peaked near 165″ hour^{-1}, corresponding to trail lengths ∼330 pixels in a single 290 s image. The most severely afflicted images were rejected or flagged so that their effect on the resulting image stacks could later be assessed. We then shifted each image to a common center and rotated the data to align celestial North with the y-axis in our pixel array. The images were then combined using a variety of statistical pixel rejection schemes. In the end, we present unclipped median combinations of the images, since the median provides a simple and robust measure of the distribution.

Figure 1 shows the image composites from the three visits, with unadorned images in the top row and contoured images in the bottom row. The projected antisolar (yellow arrows) and negative heliocentric velocity vectors (white arrows) are superimposed. The isophotes on Bennu show no evidence of preferential elongation in either the antisolar or velocity directions, and there is no evidence of a dust trail in the data, even in 2023 September, where the in-plane observing geometry would maximize the surface brightness of any such a trail. The median apparent magnitudes of Bennu from the three visits vary from V = 22.86 (2012 September), 22.60 (2012 December) to 22.17 (2023 September), as a result of the changing observing geometry (Table 1).

2.2. Time Resolved Nucleus Photometry

We obtained photometry from the WFC3 images using a circular aperture of projected radius 0.2″ (5 pixels) with sky subtraction from the median signal within a contiguous annulus extending to an outer radius of 55 pixels (2.2″). WFC3 data are afflicted with large numbers of cosmic rays. We visually inspected each image for possible cosmic ray contamination and, where found, rejected the images from further consideration. Four contaminated images were rejected. Calibration was obtained by using the WFC3 Exposure Time Calculator[1] to note that a V = 0 sun-like (G2V) source gives a count rate 4.72×10^{10} s^{-1}. This calibration is approximate, both because the F350LP filter bandpass is very broad compared to the V filter and because Bennu is slightly redder than the Sun in reflected light. Nevertheless, the resulting average apparent magnitudes are within a few $\times0.01$ magnitudes of the JPL Horizons prediction and are of sufficient accuracy for our purposes. The apparent magnitudes are listed in Table 2.

Hergenrother et al. (2013) determined the phase function of Bennu, finding a linear coefficient $\beta_V = 0.040 \pm 0.003$ magnitudes (degree)$^{-1}$ over the 15° to 96° phase angle range. We applied this phase angle correction to the apparent magnitudes from Hubble and list the resulting absolute magnitudes in Table 2. The average absolute magnitudes from the new data are compared with earlier values in Table 3. Uncertainties in the last column of the table include the errors of measurement but not uncertainty on the phase function. Given the large phase angles (up to ∼82° in UT 2023 September) the latter are dominant; for example, at $\alpha = 82°$, the 1σ uncertainty in absolute magnitude due to the ±0.003 magnitudes (degree)$^{-1}$ phase function uncertainty reaches 0.25 magnitudes. The absolute magnitudes from Hubble are ∼0.25 magnitudes brighter than the value reported from ground-based data by Hergenrother et al. (2013) but consistent with the updated value by

[1] `https://etc.stsci.edu/etc/input/wfc3uvis/imaging/`

Hergenrother et al. (2019). It is not clear whether this difference simply reflects the phase function uncertainty or the existence of a color term in the F350LP to V filter conversion.

Figure 2 shows the rotational lightcurve of Bennu phased from the HST data using a period $P = 4.2961$ hour, compared with the lightcurve from 2005 September 16 measured by Hergenrother et al. (2013) and taken from Figure 4 of Nolan et al. (2019). The latter has been shifted to best match the data from 2023. Bennu's lightcurve has three maxima per rotation, rather than the two maxima expected from rotational symmetry, because it is influenced by small scale structures (including individual boulders) on the surface. The photometric range, particularly near phase $\sim$0.5, appears smaller in the binned data from 2005 than in 2023, presumably as a result of changing viewing geometry. Despite this, and with the exception of a single measurement from 2023 September 25 (at phase 0.63) the shapes of the two lightcurves are similar and there is no ambiguity in their alignment. Error bars on the 2023 data are estimated as $1\sigma = \pm 0.03$ magnitudes. Error bars on the 2005 data are not plotted for clarity but, judging from the scatter in measurements repeated over four rotations, are likely to be at least as large. A preliminary analysis (Dr. Michael Nolan, private communication) indicates that the phase of the Bennu lightcurve supports the continuation of the spin acceleration reported by Nolan et al. (2019). We defer a detailed analysis of the spin state of Bennu to a later paper.

2.3. Dust Coma

The escape velocity from Bennu varies from nearly zero at the equator (because of centripetal acceleration) to $\sim$0.2 m s^{-1} at the poles (Jiang & Schmidt 2020)). Particles launched below the escape velocity can follow sub-orbital and bound trajectories within a Hill radius, r_{Hill}, of the body. The Hill radius is

$$r_{Hill} = q \left(\frac{\rho_B}{3\rho_\odot} \right)^{1/3} \frac{a_B}{R_\odot} \tag{1}$$

where $\rho_B = 1190 \pm 15$ kg m^{-3} and $a_B = 245$ m are the bulk density and effective radius of Bennu (Lauretta et al. 2019a), $\rho_\odot = 1300$ kg m^{-3} and $R_\odot = 7 \times 10^8$ m are the density and radius of the Sun, and $q = 0.897$ au is the perihelion distance. Substitution gives r_{Hill} = 32 km, about 130 times the radius of Bennu. Numerical integrations suggest that from 1% to 10% of ejected particles larger than 1 μm could temporarily populate the Hill sphere (Jiang & Schmidt 2020). Unfortunately, even at its closest approach to Earth ($\Delta = 0.551$ au in 2023 September c.f. Table1), the Hill sphere radius subtends only 0.08″, comparable to the 0.08″ FWHM of WFC3 data. Therefore, our WFC3 data do not have the resolution to resolve material trapped within the Hill sphere of Bennu.

In this section we seek evidence for a near-nucleus dust coma beyond Bennu's Hill sphere. Figure 3 shows, $\Sigma(\theta)$, the surface brightness averaged within concentric, circular annuli, as a function of angular distance from the photocenter, θ, with sky subtraction from the median signal in a separate annulus having inner and outer radii 50 pixel and 150 pixel, respectively. We show profiles for both months in 2012 and for 2023, with September 24 and 25 combined. All three profiles are normalized at the central pixel for ease of comparison. Peak surface brightnesses from the three epochs are $\Sigma(0°) = 18.32$ magnitudes arcsec^{-2} (2012 September), 18.05 magnitudes arcsec^{-2} (2012 December), and 17.42 (2023 September) magnitudes arcsec^{-2}, with the differences being a result of the varying observational geometry (Table 1). We estimated the sky background uncertainties, shown as $1\sigma = 2\times10^{-4}$ error bars in Figure 3, from the scatter in a series of local measurements within boxes 5×5 pixels in size, distributed around the location of Bennu in the composite data. The uncertainties result from a combination of intrinsic errors in the flat field, incomplete removal of overlapping trailed field stars and galaxies, faint interference fringes

present in some flat-fielded data and, especially, from a complex internal reflection field within the WFC3 optics. The solid black line in Figure 3 shows the HST point spread function (PSF), which we measured using reference images of sidereally guided images from the Mikulski Archive for Space Telescopes[2]. The PSF shown in Figure 3 was measured from stars in F350LP imaging data from GO 13767 (2015 May 31) and 15145 (2018 February 21) with exposure times of 485 s and 352 s, respectively.

The three profiles are in close agreement for $\Sigma(\theta)/\Sigma(0^\circ) \geq 10^{-3}$, but at fainter levels the profiles begin to diverge from each other and from the PSF. This divergence is consistent with the systematic uncertainty resulting from the background subtraction. We measured a limit to the excess brightness in the $0.5''$ to $1.0''$ radius range as <1% of the total light from Bennu. Scaling from the mean projected cross-section of Bennu, $C = 0.19$ km^2, we set an upper limit to the dust cross-section as $C = 1900$ m^2 in this annulus.

The measured ejection speeds of centimeter-sized particles, U, lie in the range $0.05 \leq U \leq 3$ m s^{-1} (Lauretta et al. 2019b). In the following, we take the geometric mean, $U \sim 0.5$ m s^{-1}, as a working estimate of the speed of centimeter sized particles. As is well known from the study of dust trails in the orbits of comets and asteroids, low velocity particles stay close to the orbit plane of the parent body and appear on the plane of the sky as thin, parallel-sided trails distinct from those of (high ejection velocity) comets.

The mass of an optically thin collection of spheres is related to their combined scattering cross-section, C, by

$$M = 4\rho_B \bar{a} C/3 \tag{2}$$

where ρ_B is the particle density and $\bar{a}$ the mean particle size. In the absence of better

[2]https://mast.stsci.edu/portal/Mashup/Clients/Mast/Portal.html

evidence we assume that the ejected particles follow a differential power law distribution such that the number of particles with radii between a and $a + da$ is $n(a)da = \Gamma a^{-q} da$, where Γ and q are constants. With this assumption, and particle sizes in the range $a_{min} \leq a \leq a_{max}$, the cross-section weighted mean radius is given by

$$\bar{a} = \frac{\int_{a_{min}}^{a_{max}} a\pi a^2 n(a) da}{\int_{a_{min}}^{a_{max}} \pi a^2 n(a) da} \tag{3}$$

The limits in the integrals of Equation 3 demand some consideration. We set $a_{max} \sim$ 10 cm based on the largest particles detected in the OSIRIS-REx data (Hergenrother et al. 2019). The choice of a_{min} is more subtle. Unfortunately, particles much smaller than a centimeter could not be detected by OSIRIS-REx regardless of their abundance, owing to the limited sensitivity of the spacecraft camera. While sub-centimeter (even sub-micron) particles can contribute to the measured HST signal if they are present, small particles can also be selectively removed from a photometry annulus by solar radiation pressure. As a crude criterion by which to assess the importance of radiation pressure clearing, we compare the distance over which a particle can be accelerated with the width of the photometry annulus. The latter, in meters, is $\Delta r = s\Delta(r_2 - r_1)$, where r_2 and r_1 are the outer and inner angular radii in arcseconds, respectively, and $s = 7.25 \times 10^5$ m (arcsec)$^{-1}$ au^{-1} is the distance subtending $1''$ from $\Delta = 1$ au. In the absence of radiation pressure, the time taken for a particle to cross this distance is

$$\tau \sim \frac{s\Delta(r_2 - r_1)}{U} \qquad [\mathrm{s}] \tag{4}$$

where U is the particle speed at ejection. For example, with $\Delta = 0.55$ au, $(r_2 - r_1) = 0.5''$, and $U = 0.5$ m s^{-1}, the crossing time is $\tau \sim 4 \times 10^5$ s (about 4.6 days). During this time, the deflection by radiation pressure is

$$\ell = \frac{1}{2}\beta g_{\odot}\tau^2 \tag{5}$$

where β is the radiation pressure efficiency factor and $g_{\odot}$ is the local gravitational acceleration towards the Sun. Combining Equations 4 and 5 gives

$$\ell = \frac{1}{2}\beta g_{\odot}\left(\frac{s\Delta(r_2 - r_1)}{U}\right)^2 \tag{6}$$

We consider that particles are deflected from the photometry annulus when $\ell \gg s\Delta(r_2 - r_1)$ and, from this inequality, we find

$$\beta \gg \frac{2U^2}{s\Delta(r_2 - r_1)g_{\odot}}. \tag{7}$$

Substituting $U = 0.5$ m s^{-1}, $\Delta = 0.55$ au, $(r_2 - r_1) = 0.5''$, and $g_{\odot} = 7.0 \times 10^{-3}$ m s^{-2} at $r_H = 0.92$ au (c.f., Table 1), gives $\beta \gg 3.6 \times 10^{-4}$. For dielectric spheres, β and the particle radius, a, are related by $\beta \sim 10^{-6}/a$, with a measured in meters (Bohren and Huffman 1983). Therefore, we conclude that particles with $a \ll 2.8 \times 10^{-3}$ m (2.8 mm) would be depleted by being swept from the photometry annulus by radiation pressure faster than they could cross it, diminishing their contribution to the scattered light. This is a crude estimate but suffices to show that submillimeter particles can be deflected on timescales shorter than the nominal aperture crossing time. On this basis, we set $a_{min} = 2.8$ mm.

Resulting solutions to Equation 3 are plotted as a function of index q, assuming a_{min} = 2.8 mm and a_{max} = 10 cm, in Figure 4 (solid black line). For comparison, we also plot three size index determinations for Bennu centimeter-sized ejecta (Hergenrother et al. 2020) (yellow triangles), and measurements of millimeter-scale meteor shower particles (Blaauw et al. 2011) (green diamonds), decameter sized sungrazing comets (Knight et al. 2010) (blue square) and submillimeter sized and larger particles released by the disintegration

of long-period comet C/2021 A1 (Leonard) (Jewitt et al. 2023) (red circle). (Note that the vertical position of the datapoints in the Figure is arbitrary). Other than a single measurement, the size distributions all lie near $q \sim 3.5$, which we adopt as the appropriate index for Bennu here. For $q = 3.5$, Figure 4 gives $\bar{a} \sim 1.7$ cm.[3] The figure also shows that the value of $\bar{a}$ is a weak function of q across the plotted range and so the choice of size distribution index is not critical here.

Lastly, the dust mass production rate, $dM/dt \sim M/\tau$, from Equations 2 and 4, can be written as

$$\frac{dM}{dt} \sim \frac{4\rho_B \bar{a} C_d U}{3s\Delta(r_2 - r_1)} \quad [\mathrm{kg\ s^{-1}}]. \tag{8}$$

As above, we take $\bar{a} = 1.7$ cm and $U = 0.5$ m s^{-1} based on particle data from OSIRIS-REx. We substitute $r_2 = 1.0''$, $r_1 = 0.5''$, finding $dM/dt \lesssim 0.12$ kg s^{-1}. This is consistent with the upper limit to mass loss in September 2018, $dM/dt \lesssim 0.15$ kg s^{-1}, deduced from in-situ measurements and using a different set of model assumptions (Hergenrother et al. 2019).

2.4. Dust Trail

Large dust particles in comets and active asteroids appear concentrated in thin, parallel-sided trails, morphologically distinct from the fan-shaped tails of (high ejection

[3]The size distribution of particles larger than 0.3 cm on the surface of Bennu was found to have q in the range from 3.3±0.1 to 4.0±0.2 (Burke et al. 2021), bracketing the index we have adopted for ejected particles. However, the ejection mechanism might well be size dependent, such that these indices are not necessarily applicable to the distribution of ejected material.

velocity) material (e.g., see examples in Jewitt (2012) and Jewitt & Hsieh (2024)). Trails are especially evident when observations are taken at a small angle from the projected orbital plane, δ_i, as is the case for our 2023 data (Table 1).

We sought evidence for a dust trail associated with Bennu. For this purpose, we transformed the image into polar coordinates centered on the Bennu photocenter, mapping the intensity at 1° angular intervals over a range of radial distances up to 100 pixels (4″). A similar approach was used by Kwon et al. (2025). The resulting azimuthal intensity map (in ADU) is shown for the UT 2023 September 24/25 data as a function of position angle in the upper two panels of Figure 5. No excess emission is evident, and the expected trail position angle (negative heliocentric velocity is marked in the figure by a vertical red line) is conspicuously empty. (Similarly, no evidence for a trail is present in the observations from 2012).

For comparison, we show in the lower part of Figure 5, the corresponding azimuthal profile of active asteroid 133P/Elst-Pizarro, also observed using WFC3 and HST (Jewitt et al. 2014). By comparison with Bennu, the trail in 133P is visually obvious, where it results from the presence of 0.2 to 10 mm sized particles following a $q \sim 3.25$ power law with a total mass loss rate of order 1 kg s^{-1}.

The visibility of a trail in optical data depends on the surface brightness and geometry of the trail, particularly on its width perpendicular to the projected orbit plane. The trail of active asteroid 133P/Elst-Pizarro, for instance, has a perpendicular width ∼1″ when observed from the orbit plane of the body. Accordingly, we simulated a Gaussian dust trail of 1″ width (FWHM) and having a range of peak surface brightnesses from $\Sigma = 23.4$ magnitudes (arcsecond)$^{-1}$ to 26.9 magnitudes (arcsecond)$^{-1}$ (Figure 6). Based on the simulations, we conclude that a Bennu trail with $\Sigma \lesssim 26.5$ magnitudes (arcsecond)$^{-1}$ would be evident in the data, which we take as an estimate of the limiting sensitivity of the 2023

September data to diffuse emission.

We integrated the signal perpendicular to the trail, then converted to the scattering cross-section of dust by scaling from the photometry of Bennu. We find that the minimum detectable trail (c.f, Panel E in Figure 6) has $C_T = 420$ m^2 (arcsecond)$^{-1}$. As in section 2.3, the distance subtended by $1''$ is $s\Delta$ and the time spent by a dust particle in crossing this distance is $\tau = s\Delta/U$, where U is the particle speed. The limit to the mass loss rate set by the non-detection of a trail is calculated using Equation 8 with $U = 0.5$ m s^{-1}, giving $dM/dt < 5.8 \times 10^{-3}$ kg s^{-1} for particles with $\bar{a} = 1$ cm. The limiting rate set by the absence of a trail is stronger than the rate set by measurement of the near-nucleus PSF because the trail has only a faint sky background whereas the wings of the PSF are affected by light from the nucleus.

For comparison (Table 4), Hergenrother et al. (2019) used spacecraft observations to set a limit to the production rate $dM/dt < 0.15$ kg s^{-1}, albeit in a limited 34 minute observational window. Emery et al. (2014) used thermal infrared observations from the Spitzer Space Telescope to infer a maximimum dust mass $M \lesssim 7 \times 10^5$ kg within 4750 km of the nucleus (see their Table 8). With $U = 0.5$ ms^{-1}, this gives $dM/dt \lesssim 0.07$ kg s^{-1}. While all mass loss rate estimates are necessarily model dependent, it is clear that mass loss from Bennu is one to two orders of magnitude weaker than from 133P/Elst-Pizarro, for which $dM/dt \sim 1$ kg s^{-1} in its active state (Jewitt et al. (2014), Hsieh et al. (2026)).

3. Discussion

Given the empirical mass loss limits summarized in Table 4, the Hubble trail limit ($dM/dt < 0.006$ kg s^{-1}) is the most sensitive of those based on direct observations. However, the Bennu rates all fall far short of the mass loss rates measured in active asteroids (where

peak values are $\sim$1 kg s^{-1}) and in comets (where rates $\sim 10^3$ kg s^{-1} are common at 1 au), consistent with the absence of measurable coma in Bennu. Indeed, Bennu is only known to be active because of the exquisite sensitivity provided by in-situ, as opposed to remote, observations. This raises the obvious possibility that many or most asteroids might be similarly active at low levels, but have escaped detection owing to the limited sensitivity of ground-based data. Assuming this to be the case, we next estimate the total rate of production of debris across the asteroid belt to be expected at the Bennu rate.

Hergenrother et al. (2020) considered the bursty nature of the mass loss events in Bennu and concluded that, while the short-term value can be much higher, the orbit-averaged mass loss rate in centimeter sized and larger particles is $dM/dt \sim 10^{-7}$ kg s^{-1}. If so, the specific mass loss rate from Bennu, represented as a sphere of radius $r_n = 245$ m, is $\mathcal{L} = (dM/dt)/(4\pi r_n^2)$. Substitution gives $\mathcal{L} \sim 10^{-7}$ kg km^{-2} s^{-1}.

We crudely estimate the cumulative mass production to be expected if all asteroids larger than radius r_{min} lose mass at the same specific rate, $\mathcal{L}$. This cumulative rate is $dM/dt(r_{min}) = C_T(r_{min})\mathcal{L}$, where $C_T(r_{min})$ is the sum of the surface areas of all asteroids larger than radius r_{min}. To calculate C_T we represent the main-belt asteroids, of total mass $M = 2.4 \times 10^{21}$ kg (Pitjeva & Pitjev 2018), as a collection of spheres with radii distributed as a $q = 3.5$ power law between minimum and maximum radii r_{min} and r_{max}, respectively, with $r_{max} \gg r_{min}$. The total (as opposed to projected) surface area is then given by

$$C_T = \frac{3M}{\rho(r_{min}r_{max})^{1/2}} \tag{9}$$

where we also take $\rho = 1190$ kg m^{-3} (the same as Bennu) as the average bulk density of the asteroids, and $r_{max} = 500$ km, the radius of the largest asteroid, (1) Ceres.

By substitution, the resulting asteroid-wide production rate is

$$\frac{dM}{dt} \sim \frac{850}{r_{min}^{1/2}} \qquad [\mathrm{kg\ s^{-1}}]. \tag{10}$$

Equation 10 clearly gives only an order of magnitude estimate and it would be unwise to over-interpret its significance. The choices of q and of r_{min} are unclear, for example, because the size distribution of the smallest asteroids is not well measured and their number is likely to be depleted (through collisions, and through rotational disruption under YORP torques) relative to a $q = 3.5$ power law. At the large size end of the distribution, the escape of impact-produced particles will be limited by the gravity of the body. Both effects suggest that dM/dt from this simple treatment is over-estimated. Nevertheless, it is safe to conclude that for any $r_{min} \gtrsim 1$ m, the active asteroids produce dust and debris at a rate at most 1% to 10% of the $\sim 10^4$ to 10^5 kg s^{-1} rate needed to maintain the Zodiacal cloud in steady state (Nesvorný et al. 2011).

Lastly, we compare the specific mass loss rate from Bennu with the same quantity in other objects in Figure 7. There, in addition to the above-mentioned range of possible values for Bennu (marked B in the figure), we show values for the active asteroid 133P/Elst-Pizarro (radius and mass loss rate 1.9 km, 1 kg s^{-1}, respectively), short-period comets 2P/Encke (2.4 km, 2000 kg s^{-1}) and 67P/Churyumov-Gersimenko (2.5 km, 600 kg s^{-1}, and long-period comet C/1995 O1 (Hale-Bopp) (32 km, 2×10^6 kg s^{-1}). For simplicity, no attempt has been made to correct the different mass loss measurements to a common heliocentric distance. Neither do we account for observations showing that peak activity levels can vary from orbit to orbit in any given object. The figure shows that the dimensions of the plotted bodies span a range of about two orders of magnitude, while the specific mass loss rates span a much more substantial range of order 10^6 to 10^8.

4. SUMMARY

We used the Hubble Space Telescope to search for mass loss from active asteroid (and former spacecraft target) (101955) Bennu from a vantage point close to its orbital plane. We use the observations to set upper limits to mass in ejected particles in the mm to cm size range. We find that

- The first limit, obtained from the near-nucleus surface brightness profile, corresponds to an upper limit to the mass loss rate $dM/dt < 0.12$ kg s^{-1}.
- The second limit, based on the absence of a low surface brightness large particle trail, is $dM/dt < 6 \times 10^{-3}$ kg s^{-1}.
- These observational limits to the activity are one to two orders of magnitude smaller than mass loss rates measured in other active asteroids.
- Bennu's orbitally averaged specific mass loss rate, $\mathcal{L} = 10^{-7}$ kg km^{-2} s^{-1}, if applicable to the surfaces of all asteroids, predicts a cumulative mass production rate $dM/dt \sim 850 r_{min}^{-1/2}$ kg s^{-1}. With $r_{min} > 1$ m, this is $\lesssim$1% to 10% of the rate needed to sustain the Zodiacal dust cloud in steady state.

We thank Jessica Agarwal, Jane Luu and the anonymous referee for comments on this paper. Based on observations made with the NASA/ESA Hubble Space Telescope, obtained from the data archive at the Space Telescope Science Institute. STScI is operated by the Association of Universities for Research in Astronomy, Inc. under NASA contract NAS 5-26555. The HST data presented in this article were obtained from the Mikulski Archive for Space Telescopes (MAST) at the Space Telescope Science Institute. The datasets on which this work is based can be found at https://doi.org/10.17909/z2xd-xn62. Support for

this work was provided by NASA through grants GO 17215 and AR 17030 from the Space Telescope Science Institute, which is operated by auRA, Inc., under NASA contract NAS 5-26555.

REFERENCES

Blaauw, R. C., Campbell-Brown, M. D., & Weryk, R. J. 2011, MNRAS, 414, 4, 3322. doi:10.1111/j.1365-2966.2011.18633.x

Bohren, C. F., & Huffman, D. R. 1983, Absorption and Scattering of Light by Small Particles (Wiley)

Bottke, W. F., Moorhead, A. V., Connolly, H. C., et al. 2020, Journal of Geophysical Research (Planets), 125, 8, e06282. doi:10.1029/2019JE006282

Burke, K. N., DellaGiustina, D. N., Bennett, C. A., et al. 2021, Remote Sensing, 13, 7, 1315. doi:10.3390/rs13071315

Chesley, S. R., French, A. S., Davis, A. B., et al. 2020, Journal of Geophysical Research (Planets), 125, 9, e06363. doi:10.1029/2019JE006363

Emery, J. P., Fernández, Y. R., Kelley, M. S. P., et al. 2014, Icarus, 234, 17. doi:10.1016/j.icarus.2014.02.005

Goossens, S., Rowlands, D. D., Mazarico, E., et al. 2021, PSJ, 2, 6, 219. doi:10.3847/PSJ/ac26c4

Glavin, D. P., Dworkin, J. P., Alexander, C. M. O., et al. 2025, Nature Astronomy, 9, 199. doi:10.1038/s41550-024-02472-9

Hartzell, C., Zimmerman, M., & Hergenrother, C. 2022, PSJ, 3, 4, 85. doi:10.3847/PSJ/ac5629

Hergenrother, C. W., Nolan, M. C., Binzel, R. P., et al. 2013, Icarus, 226, 1, 663. doi:10.1016/j.icarus.2013.05.044

Hergenrother, C. W., Maleszewski, C. K., Nolan, M. C., et al. 2019, Nature Communications, 10, 1291. doi:10.1038/s41467-019-09213-x

Hergenrother, C. W., Maleszewski, C., Li, J.-Y., et al. 2020, Journal of Geophysical Research (Planets), 125, 9, e06381. doi:10.1029/2020JE006381

Hsieh, H. H. & Jewitt, D. 2006, Science, 312, 5773, 561. doi:10.1126/science.1125150

Hsieh, H. H., Noonan, J. W., Kelley, M. S. P., et al. 2026, PSJ, 7, 5, 125. doi:10.3847/PSJ/ae64e9

Jewitt, D. 2012, AJ, 143, 3, 66. doi:10.1088/0004-6256/143/3/66

Jewitt, D., Ishiguro, M., Weaver, H., et al. 2014, AJ, 147, 5, 117. doi:10.1088/0004-6256/147/5/117

Jewitt, D., Kim, Y., Mattiazzo, M., et al. 2023, AJ, 165, 3, 122. doi:10.3847/1538-3881/acb53b

Jewitt, D. & Hsieh, H. H. 2024, In Comets III, Edited by Karen J. Meech et al. Space Science Series, University of Arizona Press, Tucson, 2024, pp. 767-798. doi:10.2458/azu_uapress_9780816553631-ch023

Jiang, Y. & Schmidt, J. 2020, Heliyon, 6, 10, e05275. doi:10.1016/j.heliyon.2020.e05275

Knight, M. M., A'Hearn, M. F., Biesecker, D. A., et al. 2010, AJ, 139, 3, 926. doi:10.1088/0004-6256/139/3/926

Kwon, Y. G., Dahlen, D. W., Masiero, J. R., et al. 2025, ApJS, 280, 2, 67. doi:10.3847/1538-4365/adfe71

Lauretta, D. S., Dellagiustina, D. N., Bennett, C. A., et al. 2019a, Nature, 568, 7750, 55. doi:10.1038/s41586-019-1033-6

Lauretta, D. S., Hergenrother, C. W., Chesley, S. R., et al. 2019b, Science, 366, 6470, eaay3544. doi:10.1126/science.aay3544

Molaro, J. L., Hergenrother, C. W., Chesley, S. R., et al. 2020, Journal of Geophysical Research (Planets), 125, 8, e06325. doi:10.1029/2019JE00632510.1002/essoar.10501385.2

Nesvorný, D., Janches, D., Vokrouhlický, D., et al. 2011, ApJ, 743, 2, 129. doi:10.1088/0004-637X/743/2/129

Nolan, M. C., Howell, E. S., Scheeres, D. J., et al. 2019, Geophys. Res. Lett., 46, 4, 1956. doi:10.1029/2018GL080658

Nuth, J. A., Abreu, N., Ferguson, F. T., et al. 2020, PSJ, 1, 3, 82. doi:10.3847/PSJ/abc26a

Pitjeva, E. V. & Pitjev, N. P. 2018, Astronomy Letters, 44, 8-9, 554. doi:10.1134/S1063773718090050

Roberts, J. H., Barnouin, O. S., Daly, M. G., et al. 2021, Planet. Space Sci., 204, 105268. doi:10.1016/j.pss.2021.105268

Takir, D., Emery, J. P., Bottke, W. F., et al. 2024, Scientific Reports, 14, 15965. doi:10.1038/s41598-024-66237-0

Walsh, K. J., Delbó, M., Bottke, W. F., et al. 2013, Icarus, 225, 1, 283. doi:10.1016/j.icarus.2013.03.005

Walsh, K. J., Ballouz, R.-L., Bottke, W. F., et al. 2024, Nature Communications, 15, 5653. doi:10.1038/s41467-024-49310-0

This manuscript was prepared with the AAS LaTeX macros v5.2.

Table 1. Journal of Observations

GO	UT Date	Exp[a]	r_H [b]	Δ [c]	α[d]	$\theta_{-\odot}$[e]	θ_{-V}[f]	δ_i[g]	ν [h]
13118	2012 Sep 17/18	40×305	1.216	0.961	53.4	99.9	282.1	0.77	236.5
13118	2012 Dec 10/11	40×305	0.952	0.962	61.9	71.3	232.5	-6.02	311.2
17215	2023 Sep 24	10×290	0.924	0.550	81.6	283.6	283.1	0.14	325.8
17215	2023 Sep 25	15×290	0.923	0.551	81.6	283.8	283.6	0.06	326.3

[a]Number of exposures × exposure time in seconds

[b]Heliocentric distance in au.

[c]Geocentric distance in au.

[d]Phase angle in degree

[e]Position angle of the projected anti-solar direction

[f]Position angle of the projected negative heliocentric velocity vector

[g]Angle of the Earth above the projected orbital plane

[h]True anomaly, degree

Table 2. Mean Magnitudes

N	Universal Date[a]	V [mag][b]	H [mag][c]
1	September 24.893	22.16 ± 0.03	20.54
2	September 24.898	22.12 ± 0.03	20.50
3	September 24.904	22.12 ± 0.03	20.50
4	September 24.909	22.16 ± 0.03	20.54
5	September 24.959	22.12 ± 0.03	20.50
6	September 24.964	22.22 ± 0.03	20.60
7	September 24.970	22.32 ± 0.03	20.70
8	September 24.975	22.34 ± 0.03	20.72
9	September 25.020	22.24 ± 0.03	20.62
10	September 25.025	22.20 ± 0.03	20.58
11	September 25.036	22.19 ± 0.03	20.57
12	September 25.041	22.22 ± 0.03	20.60
13	September 25.349	22.12 ± 0.03	20.50
14	September 25.360	22.12 ± 0.03	20.50
15	September 25.366	22.13 ± 0.03	20.51
16	September 25.371	22.16 ± 0.03	20.54
17	September 25.416	22.24 ± 0.03	20.62
18	September 25.421	22.24 ± 0.03	20.62
19	September 25.426	22.21 ± 0.03	20.59
20	September 25.432	22.15 ± 0.03	20.53
21	September 25.437	22.12 ± 0.03	20.50

Table 2—Continued

N	Universal Date[a]	V [mag][b]	H [mag][c]

[a]Universal date of the observation in 2023

[b]Apparent V magnitude and 1σ uncertainty

[c]Absolute magnitude computed from V assuming phase function 0.04 magnitudes degree^{-1}. The statistical uncertainty on H is the same as on V but the absolute uncertainty could be several $\times 0.1$ magnitude as a result of the phase correction.

Table 3. Mean Magnitudes

UT Date	ID	FILTER	mag[a]	H [b]
2012 Sep 17	GO 13118	F350LP	22.80±0.01	20.32±0.16
2012 Dec 10	GO 13118	F350LP	22.54±0.01	20.25±0.21
2023 Sep 24	GO 17215	F350LP	22.20±0.03	20.40±0.24
2023 Sep 25	GO 17215	F350LP	22.18±0.01	20.38±0.24
Hergenrother et al. (2013)	N/A	V	–	20.61±0.20
Hergenrother et al. (2019)	N/A	V	–	20.41±0.02

[a]Mean apparent magnitude within a 0.8″ radius aperture

[b]Mean absolute magnitude computed assuming phase function 0.040±0.003 magnitudes (degree)$^{-1}$ (Hergenrother et al. 2013). The quoted uncertainty is due to the combined measurement and phase angle corrections, but does not include scatter from incomplete sampling of the lightcurve at each epoch.

Table 4. Mass Loss Rates

UT Date[a]	r_H[b]	dM/dt [c]	Method[d]	Source [e]
2007 May 8	1.138	<0.07	Spitzer thermal imaging	Emery et al. (2014)
2018 Sep 11/12	1.208	<0.15	In-situ optical imaging	Hergenrother et al. (2019)
2023 Sep 24/25	0.923	< 0.12	Hubble, coma	This Work, §2.3
2023 Sep 24/25	0.923	< 0.006	Hubble, trail	This Work, §2.4
Orbit Average	–	$\lesssim 10^{-7}$	–	Hergenrother et al. (2020)

[a]UT Date of the measurement

[b]Heliocentric distance in au.

[c]Mass loss rate in kg s^{-1}

[d]Method of measurement

[e]Reference

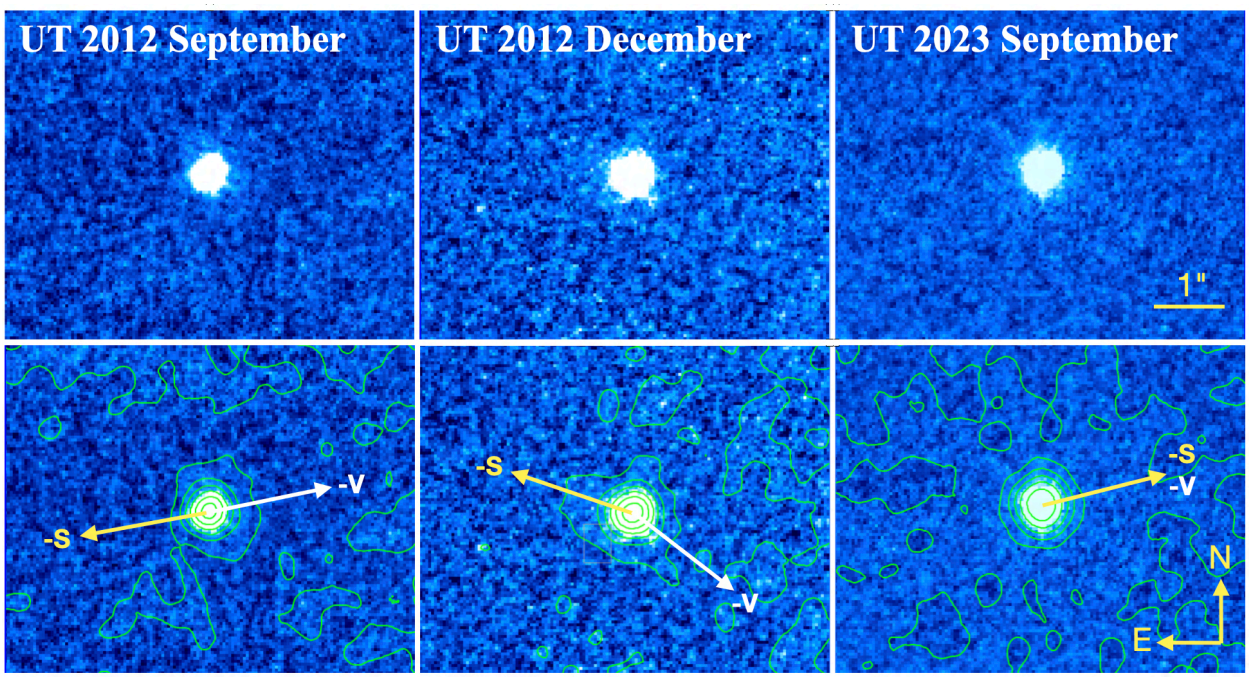

Fig. 1.— (Top row:) Composite images on three dates (Table 1) shown with a common display range from -0.01 to 0.02 adu pixel^{-1}. (Bottom row:) Same images from the top row contoured from 0.0004 adu pixel^{-1} in steps of 0.002 adu pixel^{-1}. Contours are smoothed over 8×8 pixel boxes. Yellow arrows show the projected antisolar direction while white arrows show the projected negative heliocentric velocity vector, from Table 1. The two directions are overlapping in the 2023 data. A 1″ scale is common to all panels.

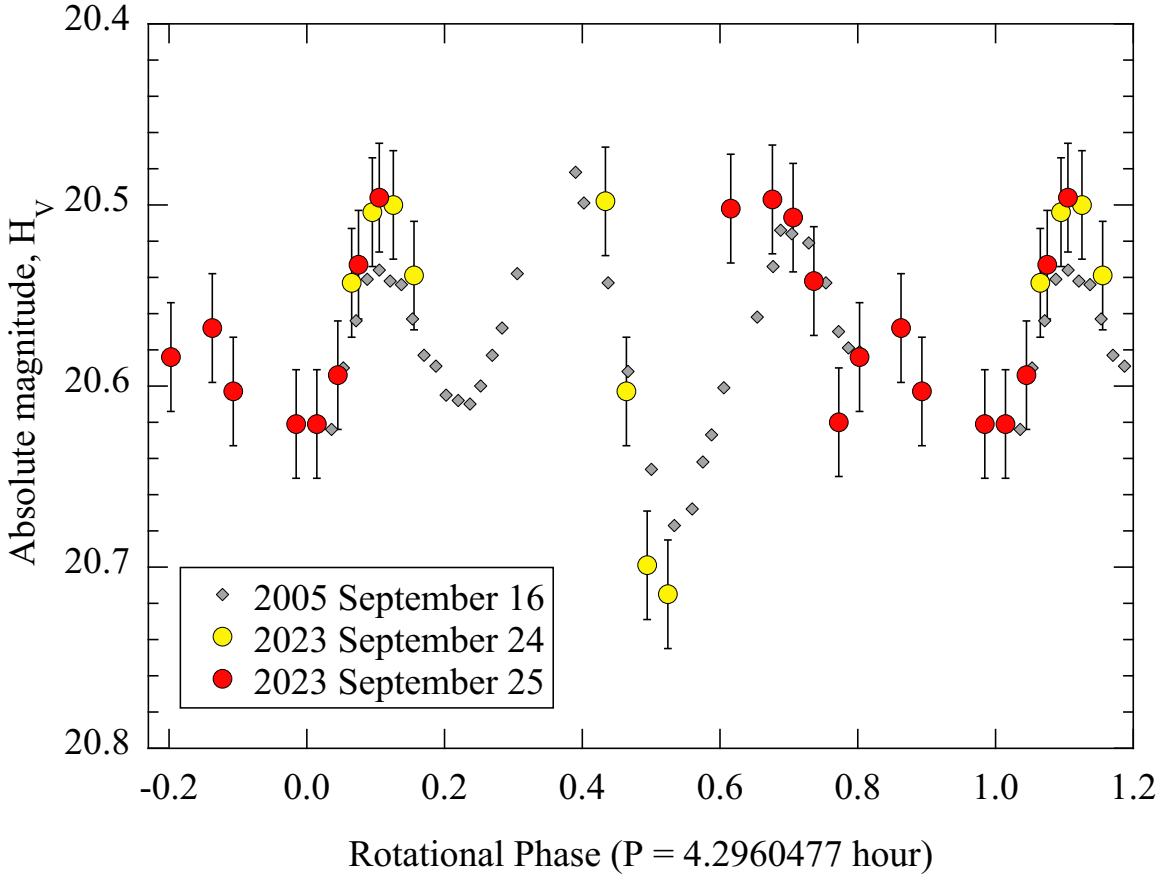

Fig. 2.— Aligned lightcurves from UT 2023 September 24 (filled yellow circles) and 25 (red circles) compared with the lightcurve of UT 2005 September 14 (small gray diamonds) from Nolan et al. (2019). Error bars on the 2023 data are $1\sigma = \pm 0.03$ magnitudes.

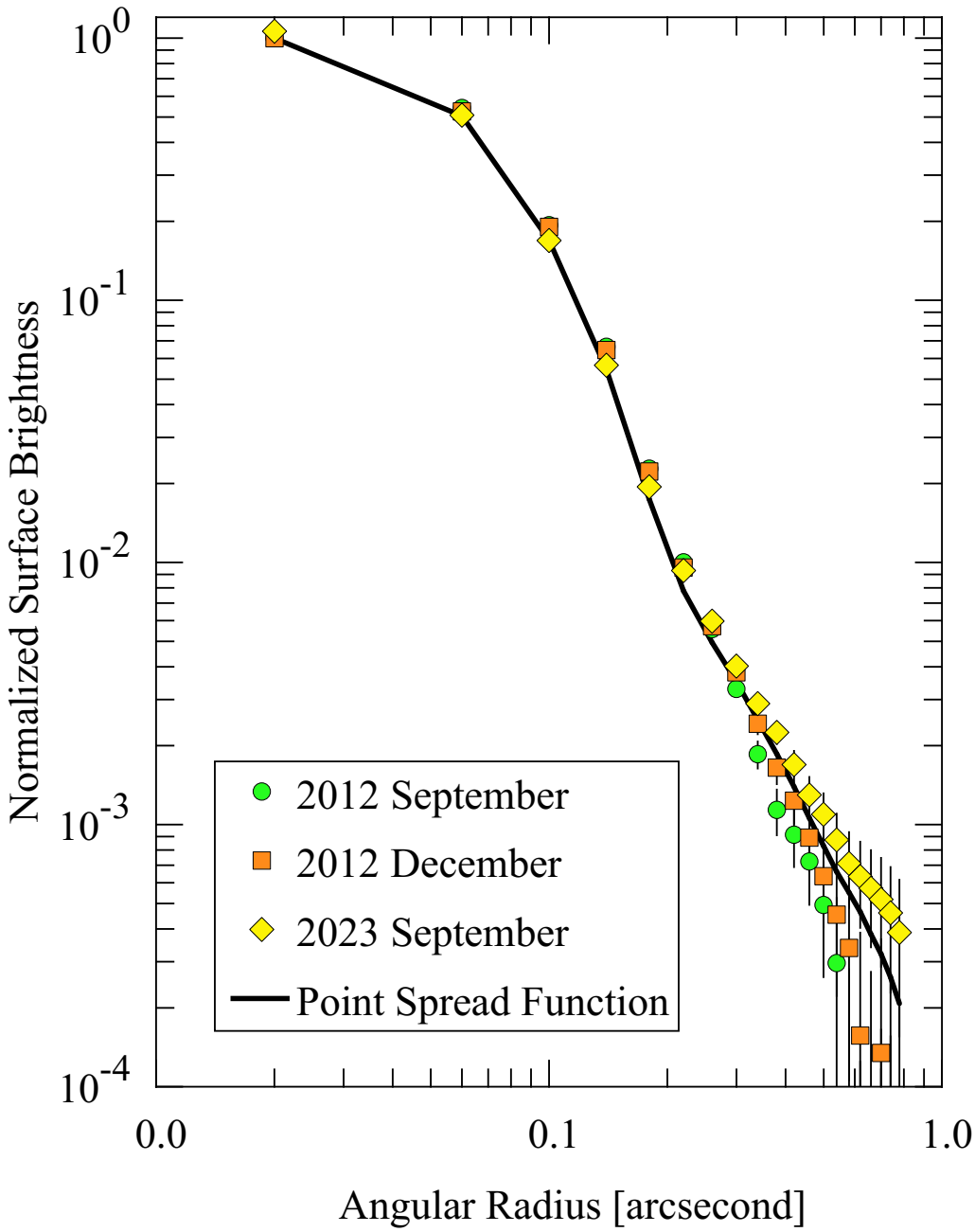

Fig. 3.— Surface brightness profiles computed from concentric circular aperture photometry. Error bars show estimated systematic sky background uncertainty $1\sigma = 2\times10^{-4}$ pixel^{-1}, estimated from spatially dispersed measurements of the residual sky level around Bennu.

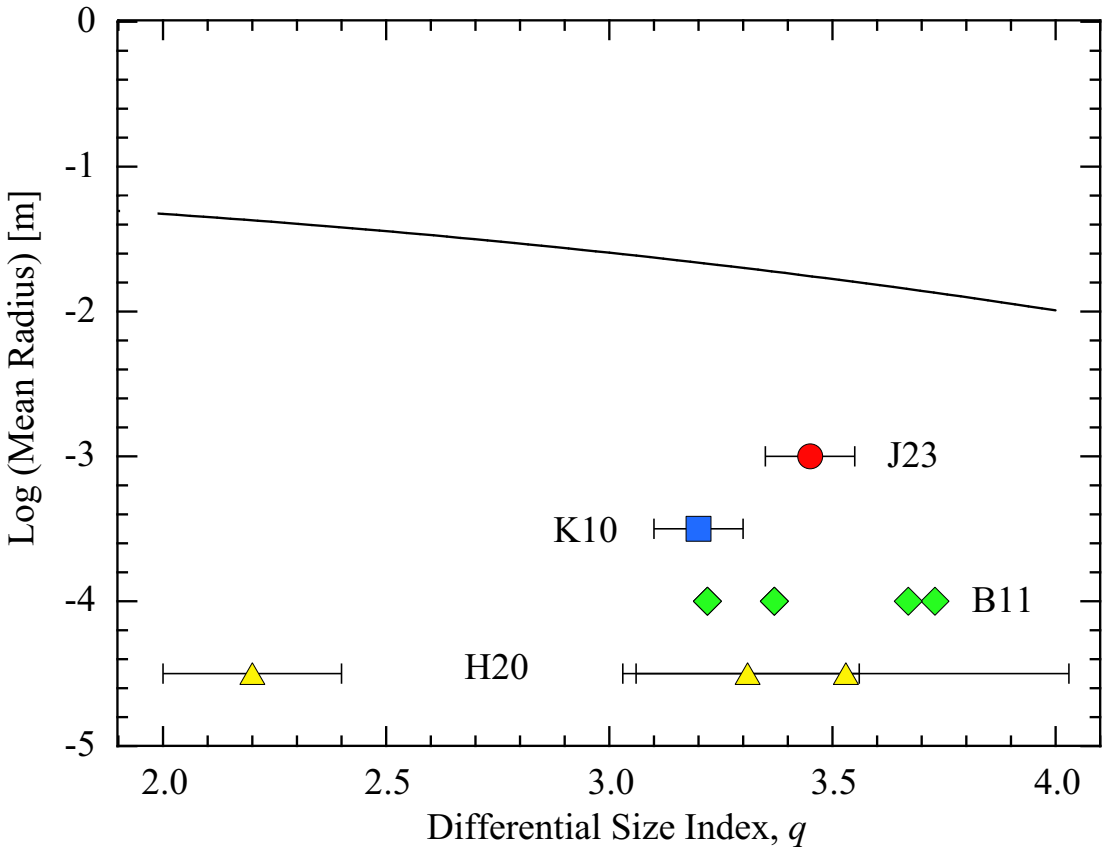

Fig. 4.— Effective mean particle radius as a function of the size distribution index, from Equation 3. For comparison, we show size index measurements from in-situ Bennu data (H20; Hergenrother et al. (2020)), meteor showers (B11: Blaauw et al. (2011)), sungrazing comets (K10: Knight et al. (2010)) and a disintegrated comet (J23: Jewitt et al. (2023)).

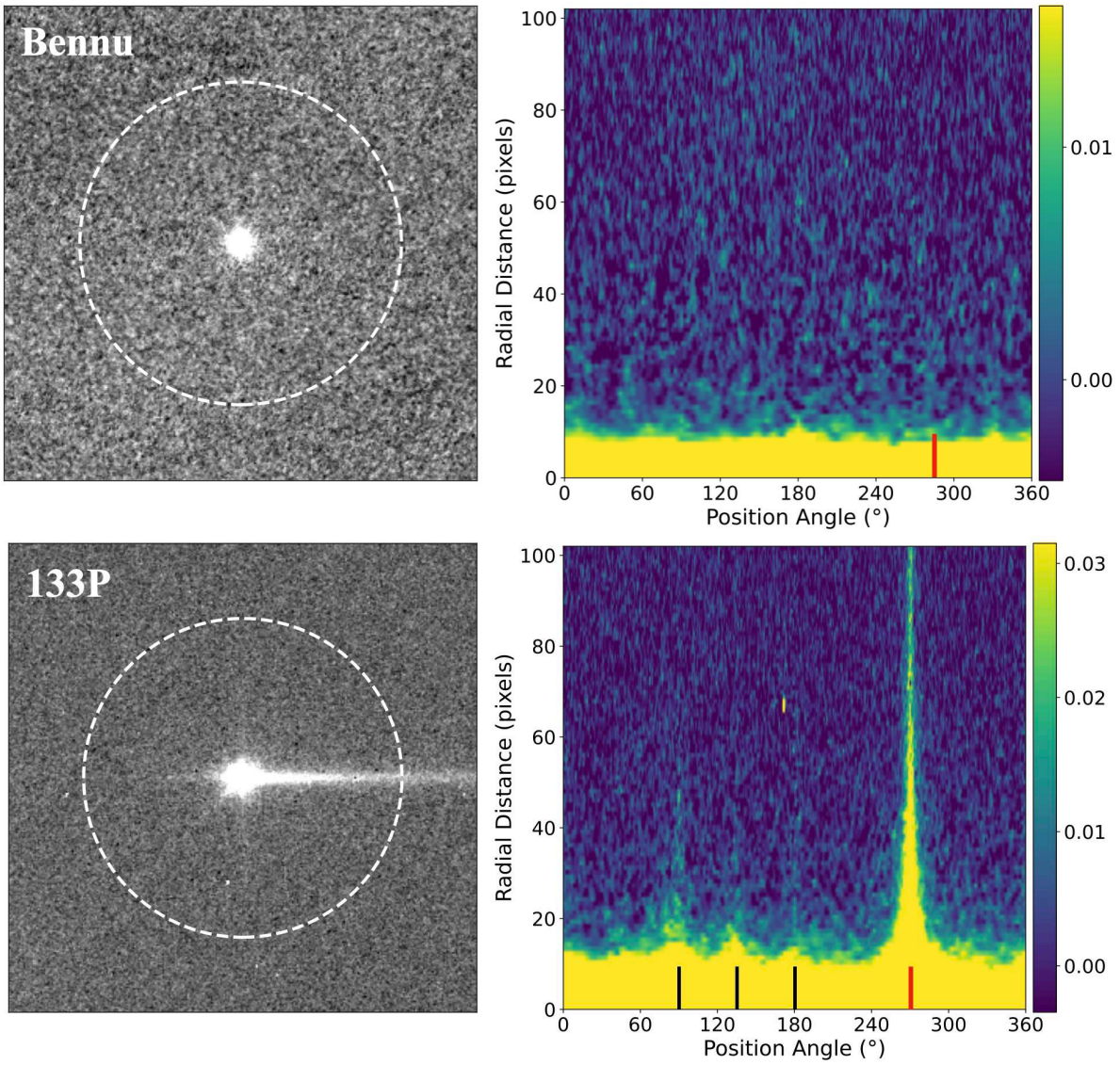

Fig. 5.— (Upper:) Composite of 21 uncontaminated Hubble images of Bennu (total exposure 6090 s) at $r_H = 0.924$ au on UT 2023 September 24/25. No significant radial structures are evident. (Lower:) Same but for a composite image of 133P/Elst-Pizarro at $r_H = 2.725$ au on UT 2013 July 10 having 3984 s total integration (from Jewitt et al. (2014)) with azimuthal plot on the right. The dotted circles in the left-hand panels for both objects have radius 100 pixels = 4.0″. A vertical red line marks the projected negative heliocentric velocity vector. Vertical black lines show significant radial image artifacts.

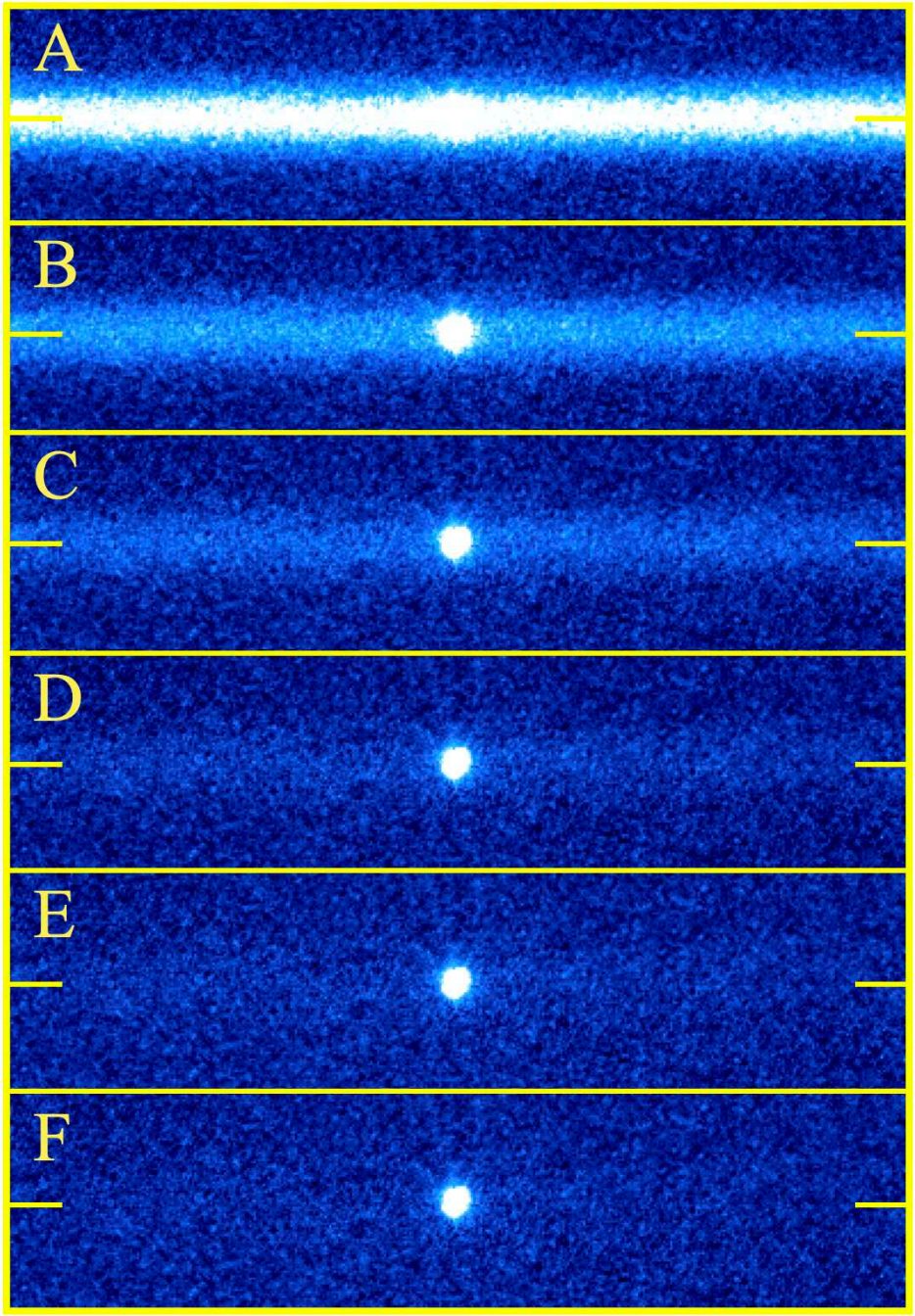

Fig. 6.— Simulated trails on UT 2023 September 24/25 having, from top to bottom, peak surface brightnesses Panel A: 23.4, B: 24.1, C: 24.8, D: 25.5, E: 26.2 and F: 26.9 magnitudes (arcsecond)$^{-2}$. Short horizontal lines to the left and right of each panel show the mid-lines of the digitally added trails. The panels are shown with a fixed stretch. The region shown in each panel is 16″ wide, centered on Bennu.

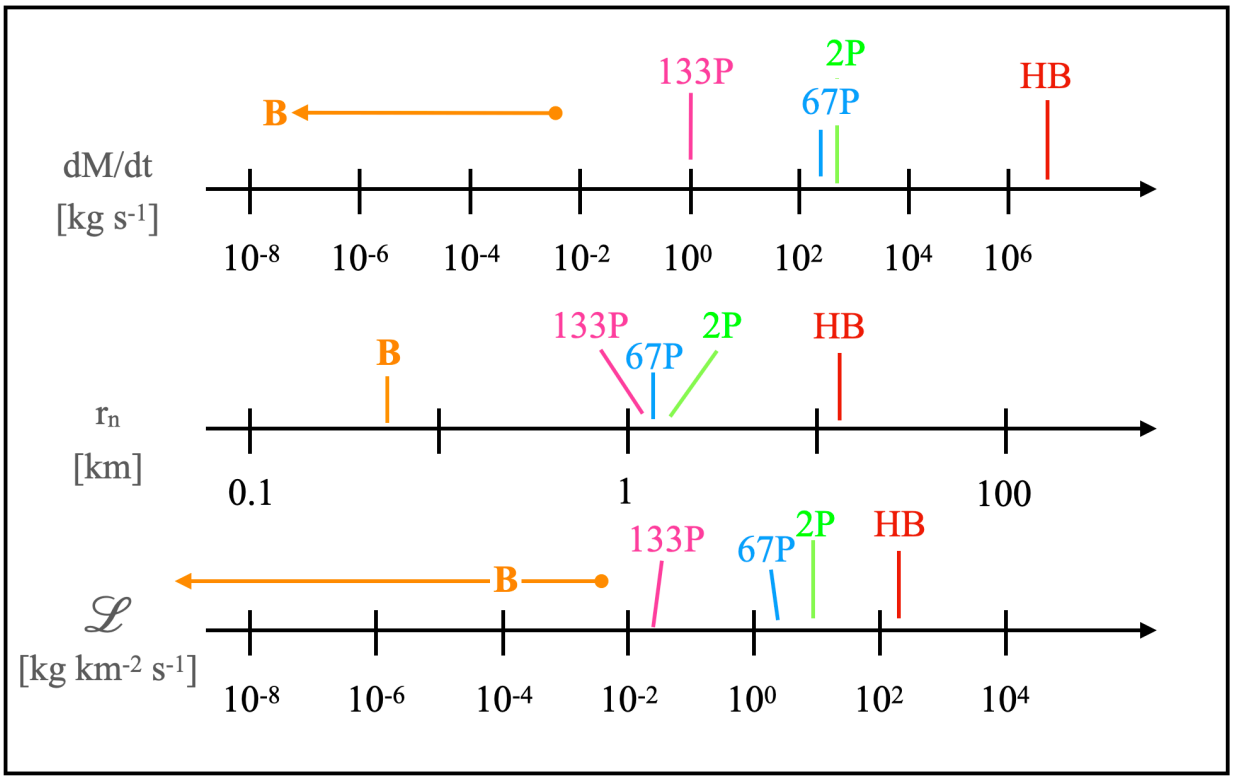

Fig. 7.— Comparison of (top) mass loss rates, dM/dt [kg s^{-1}], (middle) nucleus radii, r_n [km], and (bottom) specific mass loss rates, $\mathcal{L}$ [kg km^{-2} s^{-1}], for Bennu (B) and cometary bodies 133P/Elst-Pizarro, 2P/Encke, 67P/Churyumov-Gerasimenko and C/1995 O1 (Hale-Bopp).